The Idealized Aquaplanet Maritime Continent Barrier Effect on the MJO Predictability

HYEMI KIM[a,b] AND JAMES J. BENEDICT[c,d]

[a] *Department of Science Education, Ewha Womans University, Seoul, South Korea*
[b] *School of Marine and Atmospheric Sciences, Stony Brook University, State University of New York, Stony Brook, New York*
[c] *Rosenstiel School of Marine and Atmospheric Science, University of Miami, Miami, Florida*
[d] *Climate and Global Dynamics Laboratory, National Center for Atmospheric Research, Boulder, Colorado*

(Manuscript received 7 March 2022, in final form 22 April 2023, accepted 27 April 2023)

ABSTRACT: Studies have indicated exaggerated Maritime Continent (MC) barrier effect in simulations of the Madden–Julian oscillation (MJO), a dominant source of subseasonal predictability in the tropics. This issue has plagued the modeling and operational forecasting communities for decades, while the sensitivity of MC barrier on MJO predictability has not been addressed quantitatively. In this study, perfect-model ensemble forecasts are conducted with an aquaplanet configuration of the Community Earth System Model version 2 (CESM2) in which both basic state and tropical modes of variability are reasonably simulated with a warm pool–like SST distribution. When water-covered terrain mimicking MC landmasses is added to the warm pool–like SST framework, the eastward propagation of the MJO is disturbed by the prescribed MC aqua-mountain. The MJO predictability estimate with the perfect-model experiment is about 6 weeks but reduces to about 4 weeks when the MJO is impeded by the MC aqua-mountain. Given that the recent operational forecasts show an average of 3–4 weeks of MJO prediction skill, we can conclude that improving the MJO propagation crossing the MC could improve the MJO skill to 5–6 weeks, close to the potential predictability found in this study (6 weeks). Therefore, more effort toward understanding and improving the MJO propagation is needed to enhance the MJO and MJO-related forecasts to improve the subseasonal-to-seasonal prediction.

KEYWORDS: Madden-Julian oscillation; Numerical weather prediction/forecasting; Subseasonal variability

1. Introduction

During the past few decades, there have been great advances in predicting the Madden–Julian oscillation (MJO; Madden and Julian 1972), a dominant mode of tropical intraseasonal variability (e.g., Kim et al. 2018; Jiang et al. 2020b). The MJO manifests as a longitudinally oriented couplet of active and suppressed deep convection that migrates eastward across the equatorial Indo-Pacific. These convection anomalies represent perturbations in atmospheric heating, which in turn drive anomalous circulation and moisture patterns both locally within the tropics and remotely in the extratropics (e.g., Sardeshmukh and Hoskins 1988). Extended-range prediction of the MJO is crucial since it provides a "forecast of opportunity" for global hazardous weather events, such as extratropical cyclones, atmospheric rivers, hail, and tornadoes (e.g., Mariotti et al. 2020).

Two aspects are useful when quantifying the accuracy of MJO forecasts: prediction skill and predictability. Prediction skill indicates what is achievable in a prediction system that contains errors emanating from the imperfect model (representation of the natural system) and the initial conditions (characterization of the natural state at the start of the simulation). Error from the imperfect boundary conditions could influence the prediction skill as well. For example, MJO is modulated by lower boundary conditions (e.g., ocean–atmospheric coupled processes; DeMott et al. 2015) as well as upper boundary conditions (e.g., tropospheric–stratospheric coupling; Wang et al. 2019; Martin et al. 2021), thus the imperfect boundary conditions simulated in models could influence the MJO prediction skill. MJO predictability has been regarded as an intrinsic limit of prediction skill assuming a perfect model in which the system does not contain errors from the model formulation, but errors from initial and boundary conditions. MJO predictability is currently estimated to be 6–7 weeks, while the actual prediction skill in state-of-the-art dynamical forecasting systems ranges from 2 to 4 weeks (e.g., Kim et al. 2018).

Estimates of MJO predictability, as well as prediction skill, can evolve over time as forecast systems improve. Perfect-model experiments have provided a pathway to estimate MJO

Benedict's current affiliation: Fluid Dynamics and Solid Mechanics, Los Alamos National Laboratory, Los Alamos, New Mexico.

Corresponding author: Hyemi Kim, hyemi.kim@ewha.ac.kr

DOI: 10.1175/JCLI-D-22-0155.1

predictability. With the coarse resolution (4° × 5° horizontal grid, 17 vertical layers) NASA Goddard Laboratory for Atmospheres (GLA) global climate model (GCM), Waliser et al. (2003) conducted a perfect-model experiment with one control run and two ensembles and showed that the MJO predictability extended out to about 20–30 days for upper-level circulation and 15 days for rainfall consistent with subsequent studies (Liess et al. 2005). However, their conclusions were based on a small number of MJO events and ensemble sizes due to limited computing resources. In addition, due to weak MJO variability and poor simulation of the MJO propagation in earlier model versions, these predictability studies underestimated the true predictability. Since these studies in the early 2000s, an assessment of MJO predictability using perfect-model experiments has not been revisited. Part of the reason for this is that GCMs were not good enough for this type of "perfect-model" experiments. Great effort has been made from the numerical modeling community to better simulate the MJO and some current GCMs have improved for generations, such as the Community Earth System Model version 2.0 (CESM2, Danabasoglu et al. 2020), which shows reasonable MJO simulation to conduct perfect-model experiments (Ahn et al. 2020; Chen et al. 2022).

Concurrent with the start of the Subseasonal-to-Seasonal (S2S) forecast project (Vitart et al. 2017), studies began using initialized reforecasts of collections of models (multimodels) to estimate the MJO predictability and showed that the MJO predictability can extend to 6–7 weeks (Kim et al. 2014; Neena et al. 2014; Liu et al. 2017). These studies assessed the MJO predictability of the initialized reforecast by treating the control run (or ensemble mean) as "truth" and comparing the remaining ensemble members to the truth, similar to perfect-model experiments. However, these initialized forecasts contain significant systematic biases as the forecast lead time increases, which often causes MJO propagation to be poorly simulated (Kim 2017; Lim et al. 2018; Kim et al. 2019; Xiang et al. 2022). Therefore, a perfect-model ensemble experiment with reasonable MJO, large ensembles, and forecasts mimicking the initialized forecast procedure will help to update our current knowledge of MJO predictability. In this study we conduct perfect-model ensemble forecast experiments with the CESM2 aquaplanet.

While the performance of MJO simulation and prediction have gradually improved, one of the main hurdles that plague the modeling and forecasting communities is the so-called Maritime Continent (MC) simulation and prediction barrier (e.g., Yoneyama and Zhang 2020). Observational studies have found that more than half of strong MJO events that form over the Indian Ocean tend to weaken or dissipate when reaching the MC (Feng et al. 2015; Kerns and Chen 2016; Zhang and Ling 2017). This is due to the interaction among multiple factors, including but not limited to the effect of a persistent and strong diurnal cycle of convection over the MC (Neale and Slingo 2003; Peatman et al. 2014; Hagos et al. 2016; Ling et al. 2019), land–sea contrast that mediates the diurnal convection and modulates the background moisture distribution (Hagos et al. 2016; Ling et al. 2019; Zhou et al. 2021), the impact of steep topography on circulation (Inness and Slingo 2006; Wu and Hsu 2009), the suppression of surface latent heat flux (Maloney and Sobel 2004; Sobel et al. 2010; Kim et al. 2011), and preferential moistening to the east of MJO convection associated with the background moisture distribution (e.g., D. Kim et al. 2021). Compared to nature, most current numerical models and dynamical forecasting systems tend to overestimate the frequency of MJO events dissipating near the MC. For example, although the CMIP6 models show general improvement of MJO characteristics compared to CMIP5 models, only about 60% of CMIP6 models (20 out of 34) simulate realistic MJO propagation across the MC (Ahn et al. 2020). By comparing 17 pairs of CMIP5 and CMIP6 simulations, Chen et al. (2022) found that the improvement of MJO propagation from CMIP5 to CMIP6 is still limited. The model error in MJO propagation is partly attributed to biases in the land–sea precipitation contrast over the MC (Chen et al. 2020, 2022) and in basic-state moisture, which impacts the differential moistening process (i.e., preferential moistening to the east of MJO convection) that is essential for MJO propagation (Gonzalez and Jiang 2017; Jiang 2017; Ahn et al. 2020). In the dynamical forecasting systems, such as the models participating in the S2S project or Subseasonal Experiment project (SubX, Pegion et al. 2019), the MC barrier effect is also exaggerated which eventually limits the forecast skill of the MJO and its teleconnections. Wang et al. (2019) found that most of the S2S reforecasts show decrease of skill when prediction targets to forecast the MJO convection centered over the MC. A recent study by Xiang et al. (2022) also showed that the MJO prediction skill for events that propagate across the MC was higher than for events that dissipate over the MC. The forecasted MJO propagation signal decays quickly, thus the forecasted frequency of MJO termination before reaching the MC is higher than observed (Vitart 2017; Kim et al. 2018). The quick damping of MJO propagation signal in reforecasts is partly explained by the basic-state moisture biases (Lim et al. 2018; Kim et al. 2019). Although it is obvious that the exaggerated MC barrier effect limits the prediction of the MJO, complex interactions between the atmosphere–land–ocean system and the gradually amplifying errors of each component as lead time increases make the interpretation of the direct impact of MC on MJO prediction difficult.

In this study, we will address the sole MC barrier effect on MJO predictability with a reduced-complexity model. While previous studies have examined the importance of the MC on MJO processes by changing the MC configuration in numerical models (e.g., Tseng et al. 2017; Tan et al. 2020; Zhou et al. 2021), the MC's impact on MJO prediction and predictability has not been addressed. Studies have shown that the MJO propagation is not well forecasted in dynamical systems, but there is no quantitative measure of how much skill is lost by the existing MC barrier. In other words, how far can MJO prediction skill be extended by overcoming the exaggerated MC barrier effect? To explore the MJO predictability by MC barrier effect, we performed a perfect-model ensemble forecast experiment with an aquaplanet model configuration.

In observations and full GCMs, the surface boundary conditions are complicated with ocean, land, and mountains in the tropics, as well as seasonal changes in large-scale monsoon

systems that together impact the MJO. The use of a standard (zero-topography) aquaplanet with prescribed sea surface temperatures (SST) rules out the impact from land–sea contrast, orography, ocean–atmospheric feedbacks, and seasonality. Therefore, we can solely focus on the impact of changes in lower boundary conditions. It needs to be emphasized that an aquaplanet configuration is a highly idealized model and some aspects of the simulation appear to be somewhat unrealistic compared to the real world. However, our purpose when designing the aquaplanet experiments is to only introduce the minimum amount of complexity yet still be able to capture the most salient features of interest. As will be described in the subsequent sections, the model still does a reasonable job in simulating mean state and intraseasonal variability. Note that the goal of this study is not a direct comparison of the aquaplanet results to the real world, but rather to assess the sensitivity of MJO predictability by changing the boundary conditions in the idealized framework.

Section 2 describes the model settings and experimental design. The impacts of the prescribed SST and MC barrier on basic state and tropical modes of variability are discussed in section 3. The impact of the entrainment rate on MJO simulation is investigated as well. In section 4, we examine the MC barrier effect on MJO predictability with the perfect-model ensemble forecast experiments. Section 5 provides the summary and discussion.

2. Data and methods

a. NCAR CESM2 aquaplanet

We use the aquaplanet configuration of the National Center for Atmospheric Research (NCAR) Community Atmosphere Model Version 6.0 (CAM6), which is the atmospheric component of the CESM2. The CESM2 shows significant improvements over the previous version (Danabasoglu et al. 2020; Simpson et al. 2020). In particular, modes of tropical variability such as convectively coupled equatorial waves (CCEWs), MJO, and El Niño–Southern Oscillation (ENSO) have improved significantly (Ahn et al. 2020; Capotondi et al. 2020; Danabasoglu et al. 2020; Chen et al. 2022). The CAM6 aquaplanet is the same numerical model as CAM6 but with reduced complexity of the boundary conditions. The aquaplanet experiments serve as a framework to develop and test hypotheses beyond simpler models and distill salient features of complex models (Hoskins et al. 1999). By damping or removing processes that may be of secondary importance, atmospheric-only aquaplanet experiments have provided insights into the underlying processes of the MJO-like modes and their future changes (Inness et al. 2001; Maloney et al. 2010; Andersen and Kuang 2012; Kang et al. 2013; Arnold et al. 2015; Maloney and Wolding 2015; Leroux et al. 2016; Pritchard and Yang 2016; Shi et al. 2018; Bui and Maloney 2019; Das et al. 2019; Jiang et al. 2020a).

Here, we use the CAM6 aquaplanet on its default grid configuration: a $0.9^\circ \times 1.25^\circ$ horizontal resolution, 32 vertical levels, and a finite-volume dynamical core. The aerosol effect is removed, and carbon dioxide concentration is set to 348 ppm (Medeiros 2020). The experiments follow the aquaplanet experiment protocol (Williamson et al. 2013); the perpetual-equinox insolation (341 W m^{-2}) is used such that the seasonality is neglected, but the diurnal cycle is retained. Earth is completely covered by water and there is no sea ice or topography, thus the effect of land surface, land–sea contrast, and land–atmosphere feedbacks are absent. To verify the simulation results, daily mean data from the ECMWF interim reanalysis (ERA-Interim; Dee et al. 2011), NOAA Advanced Very High-Resolution Radiometer (Liebmann and Smith 1996) Outgoing Longwave Radiation (OLR) product from 1979 to 2017, and Global Precipitation Climatology Project 1° daily version 1.2 (GPCP-1DD; Huffman et al. 2001) from 1997 to 2015 are used.

b. Experimental design

To examine the impact of the lower boundary conditions on the simulation of basic-state and MJO activity, 10-yr perpetual runs forced by three different configurations of fixed SST are performed: control (CTRL), warm pool (WarmPool), and Maritime Continent aqua-mountain (MCaquaMtn) experiments. The CTRL run is prescribed with a zonally symmetric "QOBS" SST profile that resembles the observed zonal-mean SST structure (Neale and Hoskins 2000) defined as

$$\mathrm{SST}_{\mathrm{QOBS}} = \frac{1}{2}\left\{300\left[1 - \sin^2\left(\frac{\pi\theta}{120}\right)\right]\right\} + \frac{1}{2}\left\{300\left[1 - \sin^4\left(\frac{\pi\theta}{120}\right)\right]\right\},$$

where θ (latitude in degrees) is between 60°S and 60°N. The CTRL SST profile has a global average of 288 K. A maximum SST of 300 K on the equator falls to 273 K at 60° latitude, and uniformly 273 K from 60° to the polar caps (Fig. 1a). With this CTRL SST profile, studies have investigated variability and processes of MJO-like waves (Hsu et al. 2014; Shi et al. 2018; Jiang et al. 2020a).

The "WarmPool" experiment is conducted to test the effect of zonal SST asymmetry (Fig. 1b) on the basic state and MJO. It is well understood that MJO convective anomalies are tightly coupled to circulation anomalies over the Pacific warm pool and decouple over cooler east Pacific (e.g., Madden and Julian 1972). The MJO phase speed is also controlled by the SST distribution, thus slower over the warm pool than other ocean basins (e.g., Roundy 2012; D. Kim et al. 2021). Aquaplanet experiments forced by warm pool–like SST show a more reasonable basic state, MJO, and tropical intraseasonal variability (Andersen and Kuang 2012; Maloney and Wolding 2015; Das et al. 2019; Wu et al. 2021), although results are model dependent (Leroux et al. 2016). A 10-yr WarmPool run is conducted by keeping everything identical to CTRL except the SST distribution (Fig. 1b) which is constructed as follows: First, we take the mean of March SST (HadISST; Rayner et al. 2003) and calculate the SST departures $[\mathrm{SST}'_{\mathrm{WP}}(x, y)]$ from the zonal mean. Then, we calculate the meridional average of $\mathrm{SST}'_{\mathrm{WP}}(x, y)$ between 5°S and 5°N, resulting in a zonal profile $\mathrm{SST}'_{\mathrm{WP}}(x)$. This is further smoothed by retaining 10 harmonics in longitude $[\mathrm{SST}'_{\mathrm{WP}}(x)]$. Then, the smoothed zonal profile of SST anomalies is applied from 30°S

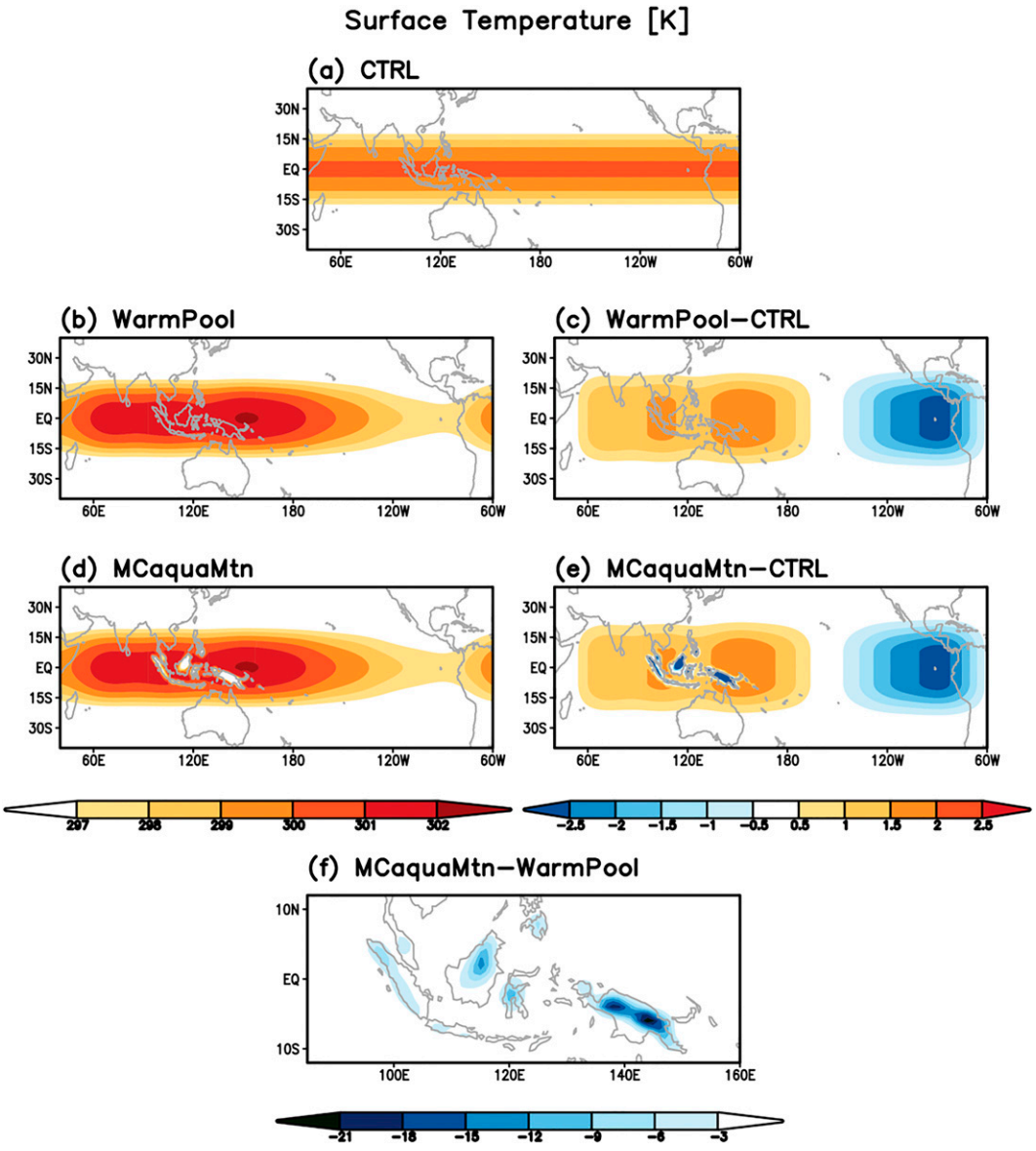

FIG. 1. The SST (K) distribution in (a) CTRL, (b) WarmPool, and (d) MCaquaMtn runs, and (c),(e) the difference from CTRL. (f) SST difference between MCaquaMtn and WarmPool.

to 30°N with a weight of 1.0 along the Equator tapered to a weight of zero poleward of 30° latitude. With this approach, the globally averaged SST and the zonal mean SST profile remain the same as CTRL. The prescribed SST pattern of the WarmPool experiment and its deviation from the CTRL run are displayed in Figs. 1b and 1c.

The "MCaquaMtn" experiment aims to explore the MC barrier effects on MJO propagation and prediction. Surface topography mimicking the MC landmasses is set to Earth-like values and remains zero elsewhere. All terrain will remain water covered; we call the terrain features "aqua-mountains." The WarmPool SST is prescribed, except that surface water temperatures over the imposed aqua-mountains decrease by a 6.5 K km^{-1} lapse rate (Fig. 1d). Note that the results show negligible difference by changing the lapse rate as 6.5, 6.0, 5.0, and 4.0 K km^{-1} (not shown).

SSTs in the MCaquaMtn simulation can be as much as 21 K colder than in the WarmPool run (Figs. 1e,f), and the air temperature in the aqua-mountain is lower than in the WarmPool case across the entire lower troposphere (not shown). With the prescribed SST, the effect of the diurnal cycle of convection is suppressed and thus is neglected. In nature, land surface temperatures in the higher terrain (e.g., Sumatra) warm faster than surrounding regions at the same elevation, which causes positive buoyancy, rising motion, and clouds/precipitation. This MCaquaMtn experiment suppresses diurnal surface temperature variance (and thus diurnal convection and related circulations) by prescribing temporally constant surface temperatures.

Although the diurnal cycle is essential for MJO as discussed in the introduction, our goal of the MCaquaMtn experiment is to keep everything as simple as possible, in the spirit of the aquaplanet framework. The aqua-mountain's elevation-dependent surface temperature substantially reduces the mean surface latent heat flux over the MC region (not shown) and the physical presence of topography disrupts low-level circulations, similar to the real Earth. Each of the perpetual runs prescribed with CTRL, WarmPool, and MCaquaMtn SSTs are simulated for 10 years (i.e., 120 months), and the simulated basic state and tropical modes of variability are compared in section 3.

3. SST and MC aqua-mountain effect on the basic state and MJO simulation

a. Basic state: Impact of SST and entrainment rate

In CTRL, where the SST is zonally symmetric, precipitation distribution follows the SST patterns and displays a maximum confined to the equator with strong meridional convergence at 850 hPa (Fig. 2a). Easterly trade winds are uniform over the tropical belt and change to westerly at about 20°S and 20°N due to the temperature gradient (Fig. 2a). Compared to the CTRL, the WarmPool SST is about 2°C higher in the Indo-western Pacific and at maximum 2.5 K colder in the eastern Pacific (Fig. 1c). The zonal SST gradient induces a pressure gradient that results in low-level convergence and maximum precipitation over the SST maximum area around 150°E (Fig. 2c, WP1 is the default CAM6 version). The general circulations are shaped by the SST distribution which mimics the Walker and local Hadley circulations, and the midlatitude jet core becomes robust (Fig. 2c). The descending branch over the Indian Ocean and associated low-level westerlies are confined to the equator. The low-level westerly and meridional convergence on the poleward side of it shifts the local maximum of precipitation off the equator, thus forming a double intertropical convergence zone (ITCZ) feature (Fig. 2c). Generally, a sharply peaked CTRL SST profile leads to a single precipitation maximum, while a flatter WarmPool SST leads to a double maximum (Leroux et al. 2016). Although the double ITCZ-like structure is a common feature of aquaplanet simulations (Williamson et al. 2013), it is highly model dependent and differs by physics packages (Leroux et al. 2016; Benedict et al. 2017). For example, in the Community Atmosphere Model version 5.0 (CAM5), the double ITCZ is produced with a zonally symmetric SST forcing (Das et al. 2019), while it is not the case in CAM6 (Fig. 2a). In general, the CAM6 WarmPool simulates improved large-scale atmospheric structure than the CTRL.

Before moving on to the MJO, we will optimize the default CAM6 model configuration for improved simulations of the basic state and tropical modes of variability by changing the cumulus entrainment rate in the WarmPool setup. Based on the moisture mode theory of the MJO, an important factor for the MJO is the sensitivity of deep convection to environmental moisture (e.g., Zhang et al. 2020; Sobel and Maloney 2012, 2013; Adames and Kim 2016; Wang and Sobel 2022). In an anomalously dry environment, entrainment will inhibit convection build-up, while a moist environment will allow buildup of deep convection (Bretherton et al. 2004). In recent dynamical forecasting systems, however, the convection–moisture relationship is not well simulated, and climate models tend to make precipitation in lower moisture regimes than what is observed (Rushley et al. 2018; Kim et al. 2019). As DeMott et al. (2007) demonstrated, the small entrainment rate in the Zhang and McFarlane (1995) convective parameterization inhibits the subsequent development of deep convection in CAM. Studies have shown that by changing the entrainment rate—thus convection–moisture coupling—simulation and prediction of tropical modes improve. For example, by doubling the entrainment rate in CAM5, intraseasonal variabilities substantially improved due to the high sensitivity of convection to free tropospheric humidity (Hannah and Maloney 2014; Bui and Maloney 2019). With an aquaplanet configuration, Peatman et al. (2018) showed that enhancing the entrainment rate improves the simulation of the CCEW and MJO. Also, MJO prediction is greatly improved in the ECMWF forecasting system when the convective parameterization is changed in a way to increase the sensitivity of deep convection to environmental moisture, which allows moisture to build up and precondition the atmosphere for deep convection (Bechtold et al. 2008; Hirons et al. 2013a,b; Vitart 2014).

Given the importance of convection–moisture coupling for MJO simulation, we change the fractional entrainment rate in the calculation of dilute convective available potential energy (CAPE). The entrainment rate is increased from 0.5, 1.0 (CAM6 default), 2.0, 5.0, and 10.0 km^{-1} in the WarmPool set up (hereafter WP0.5, WP1, WP2, WP5, and WP10, respectively). For example, 2.0 km^{-1} indicates doubling of entrainment rate (higher entrainment rate) compared to the CAM6 default value of 1.0 km^{-1}. To test the sensitivity of model simulation to entrainment rate, the model with each configuration is simulated for 3 years (36 months) and the basic-state climatology is displayed in Figs. 2b–f. As the entrainment rate increases (from Figs. 2b–f) and deep convection becomes more sensitive to the environmental moisture, the precipitation amount increases, and convection becomes generally more confined in latitude to the equator and warm pool area following the shape of the SST (Figs. 2b–f). The precipitation averaged over the tropical band (5°S–5°N, Fig. 3a) clearly shows an overall increase across the Indo-Pacific warm pool as entrainment rate increases. Almost double the amount of precipitation is simulated in WP10 compared to WP0.5 over the warm pool area (Fig. 3a). The Walker and local Hadley-like circulations also change associated with the change in precipitation amount and distribution. The low-level westerly wind over the equatorial Indian Ocean becomes weaker as the precipitation increases over the Indian Ocean (Figs. 2 and 3). Note that addressing the underlying physics of these changes is beyond the scope of this study, and the sensitivity tests aim to determine the best configuration for basic-state and MJO simulation to be used for MJO predictability study.

Over tropical oceans, precipitation increases exponentially when relative humidity reaches about 80% saturation, indicating the strong coupling between the precipitation and moisture (Bretherton et al. 2004). However, in most GCMs and

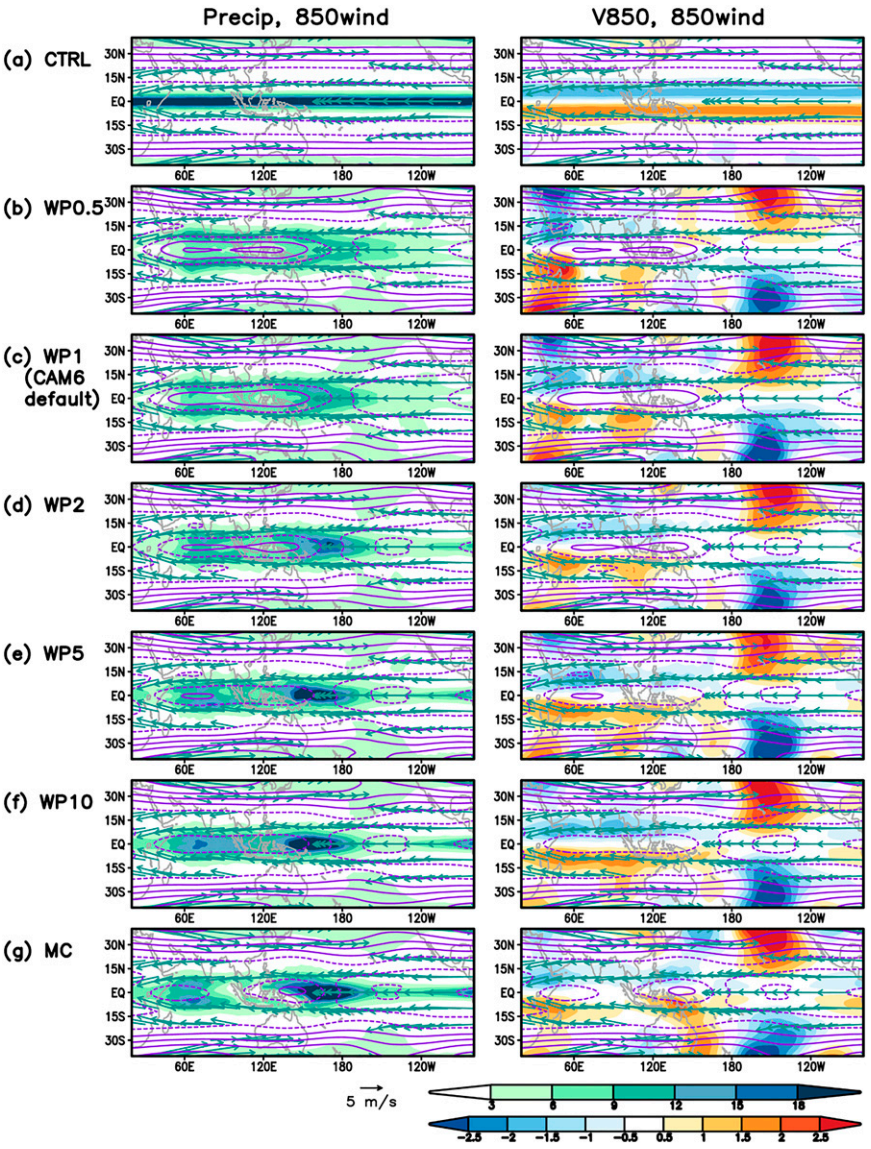

FIG. 2. Climatology of (left) precipitation (shading; mm day^{-1}) and (right) V850 (shading; m s^{-1}) with horizontal wind vectors at 850 hPa (only values larger than wind speed of 6 m s^{-1} are shown) simulated by CTRL, WarmPool with various entrainment rate, and MCaquaMtn experiments. Purple contours denote U850 (contour interval is 5.0 m s^{-1}).

S2S/SubX models, the precipitation pickup occurs earlier than the observed, meaning that precipitation occurs in less humid regimes which can impact the MJO simulation fidelity (Jiang et al. 2015; Ahn et al. 2017; Rushley et al. 2018; Kim et al. 2019). To examine the impact of the entrainment rate to moisture–precipitation coupling, the distribution of precipitation rate in each precipitable water (PW) bin is calculated over each grid point and then averaged over the warm pool (15°S–15°N, 60°E–180°) (Fig. 4). In observations (GPCP and ERAI), precipitation occurs when PW is above 45 mm, and increases exponentially beyond that. In the default CAM6, precipitation tends to occur earlier and in a drier regime than that seen in observational estimates over all PW bins. When the entrainment rate is increased, thus precipitation becomes more sensitive to environmental moisture, precipitation occurrence shifts to a higher PW regime and becomes closer to the observation (Fig. 4). Given that the higher entrainment rate simulates reasonable mean state and precipitation–moisture relationship, which is crucial for MJO simulation, we will use the WP10 (10-times-larger entrainment rate than the default CAM6) for the WarmPool and MC experiments for the rest of the analysis, although a 10-times-larger entrainment rate is somewhat too high and could directly and indirectly impact simulation of other phenomena.

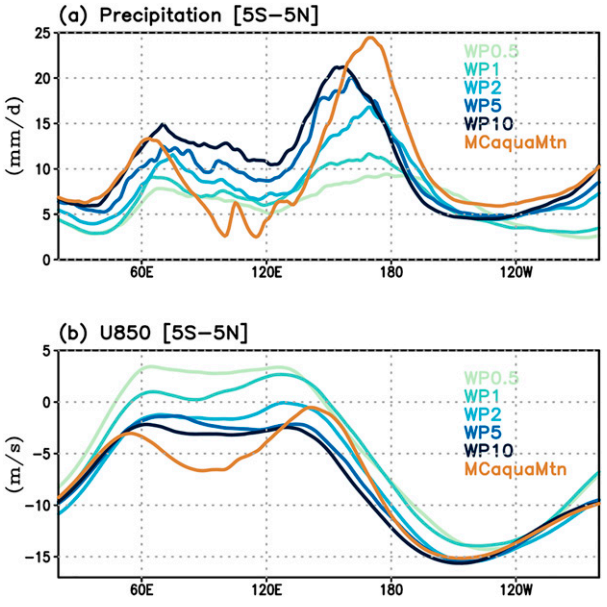

FIG. 3. (a) Precipitation (mm day^{-1}) and (b) U850 (m s^{-1}) averaged over 5°S–5°N for each WarmPool entrainment-rate sensitivity simulation (increase from light green to dark blue line) and MCaquaMtn simulation (brown line).

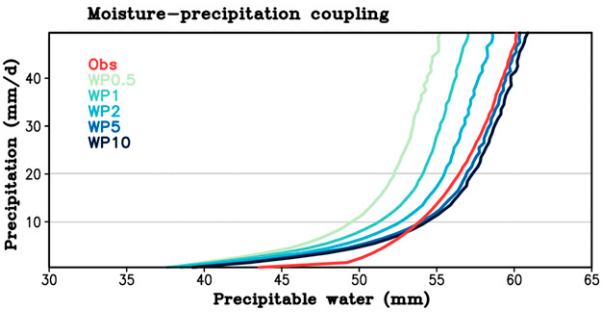

FIG. 4. Distribution of daily total precipitation rate in each precipitable water (mm) bin in the WarmPool entrainment-rate sensitivity simulations (increase from light green to dark blue line) averaged over the Indo-Pacific warm pool (15°S–15°N, 60°E–180°). "Obs" indicates GPCP and ERAI (red line). The gray lines indicate precipitation at 10 and 20 mm day^{-1}.

b. *Tropical modes of variability: CCEWs and MJO*

To assess the impact of the SST distribution to CCEWs and MJO simulation, we perform a wavenumber-frequency spectral analysis using daily OLR data averaged over the equatorial band (15°S–15°N) and remove a smooth empirical background noise spectrum (Wheeler and Kiladis 1999). Figure 5 shows the ratio of the power of the wave to the total power in the symmetric components about the equator. The signal is statistically significant if the ratio is above 1.2 similar to Wheeler and Kiladis (1999). In CTRL (Fig. 5b), the simulated Kelvin wave has slower speed than the observation and the equatorial Rossby (ER) wave is weaker than the Kelvin wave signal, consistent with many aquaplanet experiments using the zonally symmetric SST profile (Williamson et al. 2013; Leroux et al. 2016). An unrealistically strong westward signal in the antisymmetric component is simulated (not shown) due to the substantially stronger the background easterly flow (Figs. 2a,f), consistent with previous aquaplanet study (Shi et al. 2018). When the warm pool SST is prescribed, CCEWs become closer to the observed (Fig. 5c), in general. The Kelvin wave becomes faster, ER power increases, and spurious westward waves in antisymmetric component reduce substantially (not shown) compared to CTRL. The moisture source determined by the SST distribution may influence the Kelvin and ER wave coupling (Rui and Wang 1990; Kang et al. 2013), thus making them more realistic.

Studies on aquaplanet simulations with zonally symmetric SSTs have shown various ranges of MJO fidelity. Only half of models capture the MJO power, indicating that the ability to simulate MJO and more generally CCEWs depends on a model's ability to accurately represent subgrid-scale convection and the mean state (Leroux et al. 2016). With the zonally symmetric SST in CAM5, the MJO-like signal is not well simulated and the MJO variability is concentrated on wavenumber 1 only (Das et al. 2019). In CAM6, the MJO-like mode is better captured in the CTRL run with the largest power concentrated broadly on wavenumbers 1–5 and at low frequency (lower than 0.0625 cycles day^{-1}) (Fig. 5b). When the WarmPool is added, the power in the MJO-like wave becomes stronger but the maximum is shifted to higher frequency than the CTRL and concentrated at wavenumbers 1–3 (Fig. 5c). To assess the robustness of MJO eastward-propagating feature, the east-to-west ratio (E/W ratio) is obtained by dividing the sum of spectral power over the "MJO band" (30–60 days, wavenumbers 1–3) by that of its westward-propagating counterpart following Ahn et al. (2017). The observed E/W ratio is about 2.4 for all seasons in observations (Fig. 5a). The CTRL run shows too strong E/W ratio (3.4) due to excessive east power over the MJO band, while WarmPool shows weaker (1.8) than the CTRL mostly due to the increase of westward power (Fig. 5c). The E/W ratio in the WarmPool is like most CMIP models (Ahn et al. 2017). The MJO-like mode in CTRL appears similar to observations in spectral space (Fig. 5b), but in physical space this mode is driven by stronger surface latent heat fluxes to the east of its deep convective center (WISHE mode) which is inconsistent with the observed MJO (Shi et al. 2018). Therefore, higher frequency of the MJO-like mode in WarmPool is acceptable for the simple aquaplanet framework, given that 1) its driving mechanisms are more realistic than in those in CTRL (next section) and 2) we must remember that the aquaplanet design is highly simplistic and we should not expect a perfect match with real world.

To examine the MJO-like variability in the WarmPool run, the Real-Time Multivariate MJO (RMM; Wheeler and Hendon 2004) index is calculated with the OLR and zonal wind at 850 and 200 hPa. Following Wheeler and Hendon (2004), we do not filter the daily variables for Fig. 6, but intraseasonally filtered data produce similar results (not shown). Figure 6 shows the two leading eigenvectors of the combined empirical orthogonal function (CEOF) in the observation and WarmPool simulation. Two modes together explain about 25% and 32% of the total

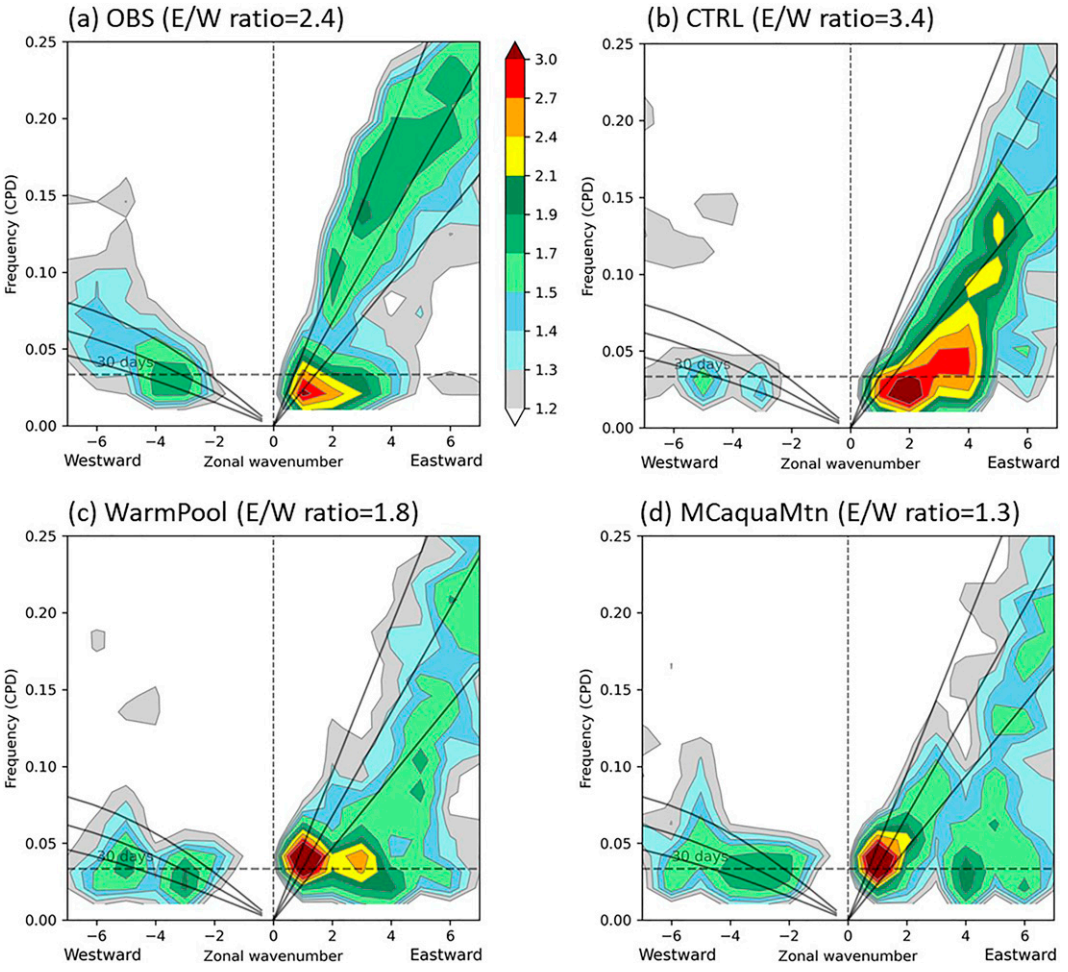

FIG. 5. The symmetric OLR power spectrum ratios of tropical waves to the background power in the wavenumber–frequency domain for (a) observation, (b) CTRL, (c) WarmPool, and (d) MCaquaMtn simulations. The power spectra are calculated based on the OLR averaged between 15°S and 15°N. The theoretical dispersion curves for the equivalent depths of 12, 25, and 50 m are superimposed. The ratio above 1.2 (indicated by the color) indicates where the spectral signatures are statistically significant at the 95% confidence level. The E/W ratio is added above each panel.

variance in observation and in WarmPool run, respectively. The daily time series of normalized principal components (PC) of the CEOF are defined as the RMM1 and RMM2 index. The observed first mode shows the negative OLR centered at about 90°E, while it extends to 150°E in the simulation. In the second mode, the model captures the convection peak near 130°E and associated low-level convergence and upper-level divergence (Fig. 6). Overall, despite the simplified model configuration, convection and the associated baroclinic circulation structures are well simulated compared to many contemporary GCMs (Ahn et al. 2017).

The two-dimensional pattern of the MJO-like mode is presented with the MJO phase composites (Fig. 7). The MJO composite maps in WarmPool run are computed with the 20–100-day filtered anomalies of OLR and horizontal wind at 850 hPa as a function of MJO phase defined by the simulated RMM index. The eastward propagation signal is simulated with strong MJO activity over the warm pool and decay of MJO signal over the eastern Pacific cold tongue (Fig. 7) [the corresponding observation can be found in Kim et al. (2018, their Fig. 1)]. Overall, as hypothesized, the WarmPool run simulates improved basic state, tropical modes of variability, and eastward propagation of MJO-like waves. Therefore, we will use this configuration to understand the MJO predictability and compare it with the MCaquaMtn run.

c. *MC barrier effect on the basic state and MJO*

The main objective of this study is to understand the MC barrier effect on MJO variability and predictability. In this subsection, we will compare the basic state and tropical modes of variability in the MCaquaMtn experiment. By prescribing the MC aqua-mountain, a sharp decrease in precipitation amount is seen over the Maritime Continent (Figs. 2g and 3a). Total amount of precipitation is reduced about 12 mm day^{-1} at

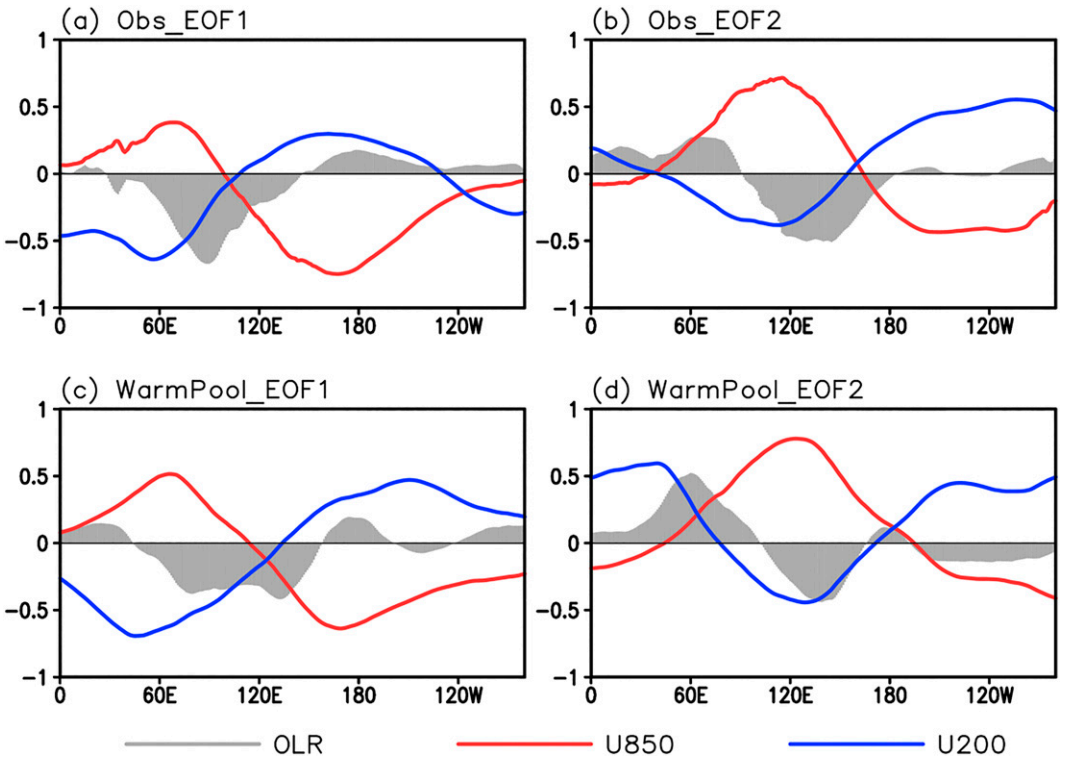

FIG. 6. First two eigenvectors of combined EOF analysis of 15°S–15°N-averaged normalized daily OLR (gray shading), U850 (red solid line), and U200 (blue solid line) anomalies for (top) observation and (bottom) WarmPool run. EOFs are indicated as normalized amplitude.

maximum over the MC region compared to the WarmPool simulation (WP10) (Fig. 3a). The reduction of the mean precipitation in MCaquaMtn run over the MC region is likely attributed to the reduced surface fluxes (not shown) which could reduce available moisture and precipitation in the MC region. The disruption of low-level convergence by the physical presence of the mountains might act as a secondary effect (Figs. 2f,g). The lack of convection near the MC splits the precipitation into two local maxima—one in the western Pacific and the other in the western Indian Ocean—along with low-level wind changes associated with the convective activities (Figs. 2g and 3b). The E/W ratio in the MCaquaMtn is about 1.3 (Fig. 5c), weaker than the WarmPool (1.8) mostly due to the decrease of eastward power.

Figure 8 shows the tropically averaged (5°S–5°N) daily mean total precipitation in randomly selected periods of 500 consecutive days (Figs. 8a–c) and the standard deviation of 20–100-day filtered total precipitation over the entire 120 months period (Figs. 8d–f) in CTRL, WarmPool and MCaquaMtn. In the CTRL run, precipitation is distributed over the entire tropical belt due to the zonally uniform SST (Fig. 8a). In the WarmPool run, the convective activity is confined to the warm pool and weakens substantially to the east of the date line where the SST reduces sharply (Fig. 8b). The MCaquaMtn run does not simulate strong convective activities over the aqua-mountain (Fig. 8c). The 20–100-day filtered variability is uniform over the tropics in CTRL run, confined to the warm pool in WarmPool run, and is split into two maxima on either side of the MC area in the MCaquaMtn run (Figs. 8d–f). The results clearly show that the MC aqua-mountain acts as a barrier for convective activity.

Hereafter, we will only compare WarmPool and MCaquaMtn to examine the MC barrier effect on MJO propagation. To compare the behaviors of anomalous convection before and after it peaks over the Indian Ocean, 10°S–10°N averaged intraseasonal (i.e., 20–100-day bandpass filtered) OLR and U850 anomalies are correlated with a reference Indian Ocean (10°S–10°N, 60°–90°E) intraseasonal OLR time series. The results are plotted in a lag–longitude map for WarmPool and MCaquaMtn runs (Fig. 9). The eastward-propagating MJO-like signals are well simulated in the WarmPool run with a near-quadrature phase relationship between convection and low-level circulation (Fig. 9a) similar to observation. When the MC barrier effect is added, the propagating convective signal from the Indian Ocean is blocked around 100°E where the aqua-mountain influences the MJO propagation (Fig. 9b). The circulation anomalies also become weaker than the WarmPool. Results from the MCaquaMtn run clearly indicate that the aqua-mountain acts as a barrier for MJO eastward propagation.

Multiple factors may contribute to the barrier effect. The disrupted mean low-level flow and reduced surface fluxes suppress the convective activity overall in the vicinity of MC, and thus prevent the MJO from maintaining its amplitude as it propagates. Also, a drier atmosphere over the MC area (Fig. 2g) does not support positive horizontal moisture advection to the east

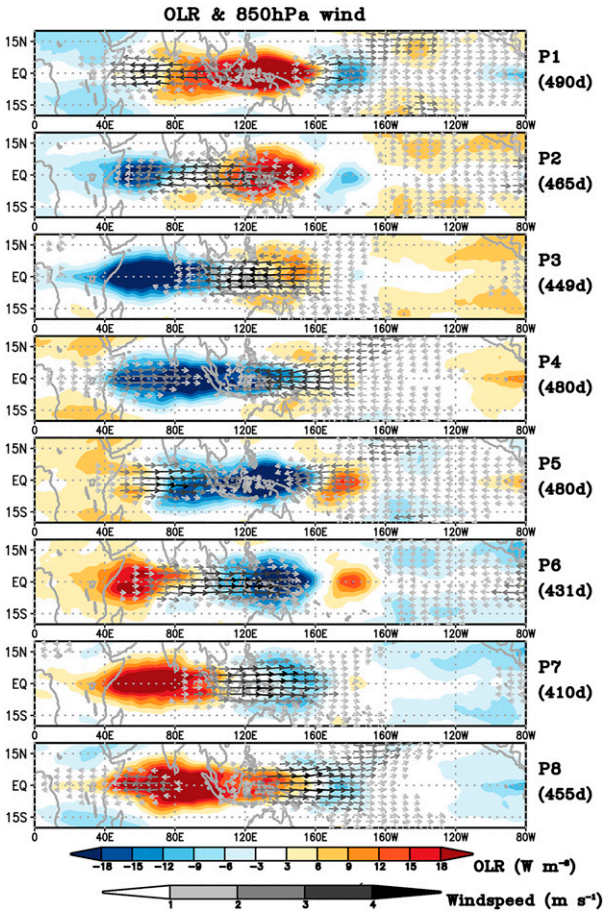

FIG. 7. MJO life cycle composite of 20–100-day filtered OLR (shading) and 850 hPa horizontal wind (vectors) anomalies in phases 1 to 8 (P1–P8) from the WarmPool experiment. The number of days falling within each phase is given in the parenthesis.

of the convection, which is crucial for MJO eastward propagation (e.g., Jiang et al. 2020b). Thus, the MJO signal from the Indian Ocean decays quickly as it propagates over the MC area where the moisture supply is not enough to maintain the MJO. Overall, the convective activity over the Indian Ocean is suppressed (Figs. 8c,f), likely due to strong low-level easterly flow blowing over the Indian Ocean from the MC region (Fig. 2g) which advects dry air to the west of MC and suppresses the convective activity, limiting MJO initiation. Detailed examination of plausible mechanism warrants further analysis.

4. Maritime Continent barrier effect on MJO predictability

a. *Perfect-model ensemble forecast experiments and evaluation metrics*

To understand the MC barrier effect on MJO predictability, perfect-model ensemble forecast experiments with and without the MC barrier are performed via two steps (Fig. 10): step 1 is the perpetual run and step 2 is the perfect-model ensemble forecast. In step 1, we perform a 10-yr perpetual run with WarmPool SST and save the restart files every 10 days. The analysis of the WarmPool run (WP10) examined in section 3 is based on this experiment. This control perpetual run is considered as truth. In step 2, we use the restart files from step 1 as atmospheric initial conditions and integrate the model for 45 days. Each 45-day forecast consists of 10 ensembles that are generated by perturbing the temperature randomly in the initial conditions (the parameter "*pertlim*" is used to produce the perturbation). Then, the 45-day forecasts are compared with the truth. This forecast experiment is performed based on the 10-yr perpetual WarmPool run, thus we have a total of 360 cases of 45-day forecast sets (10 years × 36 cases per year). In step 2, forecast experiments are conducted with two types of boundary conditions: WarmPool and MCaquaMtn SST used in section 3. The predictability analysis for both WarmPool versus MCaquaMtn run will provide us the estimate of MJO predictability and the predictability loss due to the MC barrier.

The MJO prediction skill is assessed in a similar way to operational forecasts by using conventional evaluation metrics (Kim et al. 2018). The forecasted anomalies from both WarmPool and MCaquaMtn runs are projected onto the eigenvectors of the observed CEOF (Figs. 6a,b) and normalized to obtain the forecasted RMM indices. Note that when the CEOF eigenvectors from model simulations are projected to forecasted anomalies, results of predictability are almost identical. The RMM forecast is compared between the truth (i.e., perpetual run from WarmPool) and ensemble forecasts from WarmPool and MCaquaMtn using four metrics: the bivariate correlation coefficient (BCOR), bivariate root-mean-square error (BMSE), signal, and noise (H. Kim et al. 2018, 2021; Lim et al. 2018) defined as

$$\mathrm{BCOR}(\tau)=\frac{\sum_{t=1}^{N}[T_1(t)F_1(t,\tau)+T_2(t)F_2(t,\tau)]}{\sqrt{\sum_{t=1}^{t=N}[T_1^2(t)+T_2^2(t)]}\sqrt{\sum_{t=1}^{t=N}[F_1^2(t,\tau)+F_2^2(t,\tau)]}}, \tag{1}$$

$$\mathrm{BMSE}(\tau)=\frac{1}{N}\sum_{t=1}^{N}\{[T_1(t)-F_1(t,\tau)]^2+[T_2(t)-F_2(t,\tau)]^2\}, \tag{2}$$

$$\mathrm{Signal}\ (\tau)=\frac{1}{N-1}\sum_{t=1}^{t=N}[\overline{F_1(t,\tau)}^2+\overline{F_2(t,\tau)}^2], \tag{3}$$

$$\mathrm{Noise}\ (\tau)=\frac{1}{N(E-1)}\sum_{t=1}^{t=N}\sum_{e=1}^{E}[\overline{F'_{1,e}(t,\tau)}^2+\overline{F'_{2,e}(t,\tau)}^2], \tag{4}$$

where $T_1(t)$ and $T_2(t)$, respectively, are the RMM1 and RMM2 from the truth at time t, and $F_1(t,\tau)$ and $F_2(t,\tau)$ are the forecasted RMM1 and RMM2 at time t with a lead time of τ days. The overbar indicates the ensemble mean and prime denotes individual ensembles' deviations from the ensemble mean. Signal refers to the variability of the ensemble

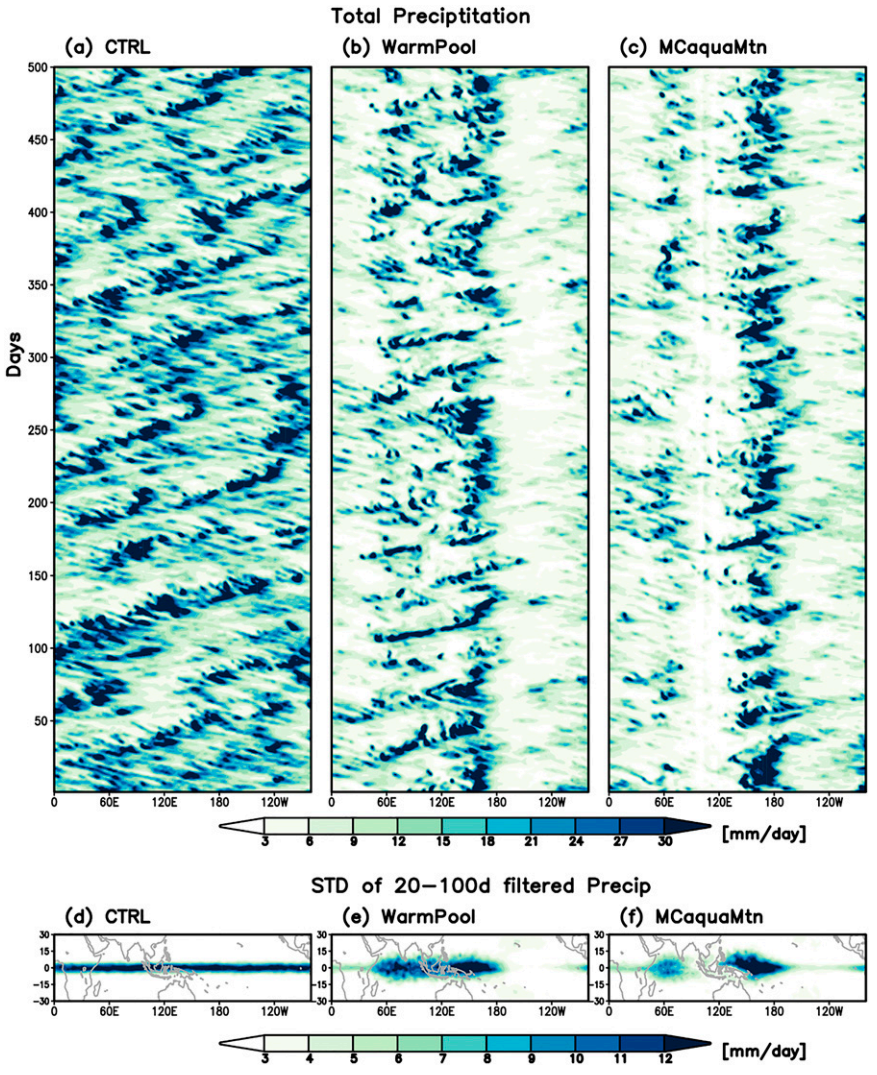

FIG. 8. Total daily precipitation (mm day^{-1}) averaged over 5°S–5°N during 500 consecutive days in (a) CTRL, (b) WarmPool, and (c) MCaquaMtn experiments. Standard deviation of 20–100-day filtered daily total precipitation calculated over 120 months in (d) CTRL, (e) WarmPool, and (f) MCaquaMtn experiments.

mean forecast and noise refers to the variability of individual forecasts around the ensemble mean (i.e., ensemble spread). E and N denote the number of ensemble members and the number of forecasts, respectively (here, $E = 10$ and $N = 360$). Note that the results are not sensitive to initial MJO amplitude, therefore we use all forecasts regardless of the initial MJO amplitude to have sufficient sample size.

b. *Maritime Continent barrier effect on MJO predictability*

The MJO predictability in the WarmPool and MCaquaMtn experiments are compared in Fig. 11. When taking BCOR = 0.5 as a reference, the ensemble-mean shows an approximately 6-week (day 40) MJO forecast skill in the WarmPool run (Fig. 11a), consistent with the theoretical estimate of MJO predictability found in earlier GCM studies using Earth-like configurations (Kim et al. 2014; Neena et al. 2014). When the MC barrier is added, the MJO propagation is interrupted by the MC and the skill decreases to 4 weeks (day 28), approximately 12 days less due to the MC barrier (Fig. 11a). The reduced skill is likely due to the aqua-mountain that makes the processes for MJO propagation harder to predict in the MCaquaMtn run. Ensemble averaging removes errors emanating from the atmospheric initial uncertainties in the single-member forecasts. In WarmPool, BCOR increases about 7 days in the ensemble-mean than the average of single-member ensembles (Fig. 11a). However, in the MCaquaMtn, ensemble mean skill increases only about 3 days over the single-member mean, indicating that taking the ensemble mean is not as effective as the WarmPool. This is likely due to the large spread among ensembles in the

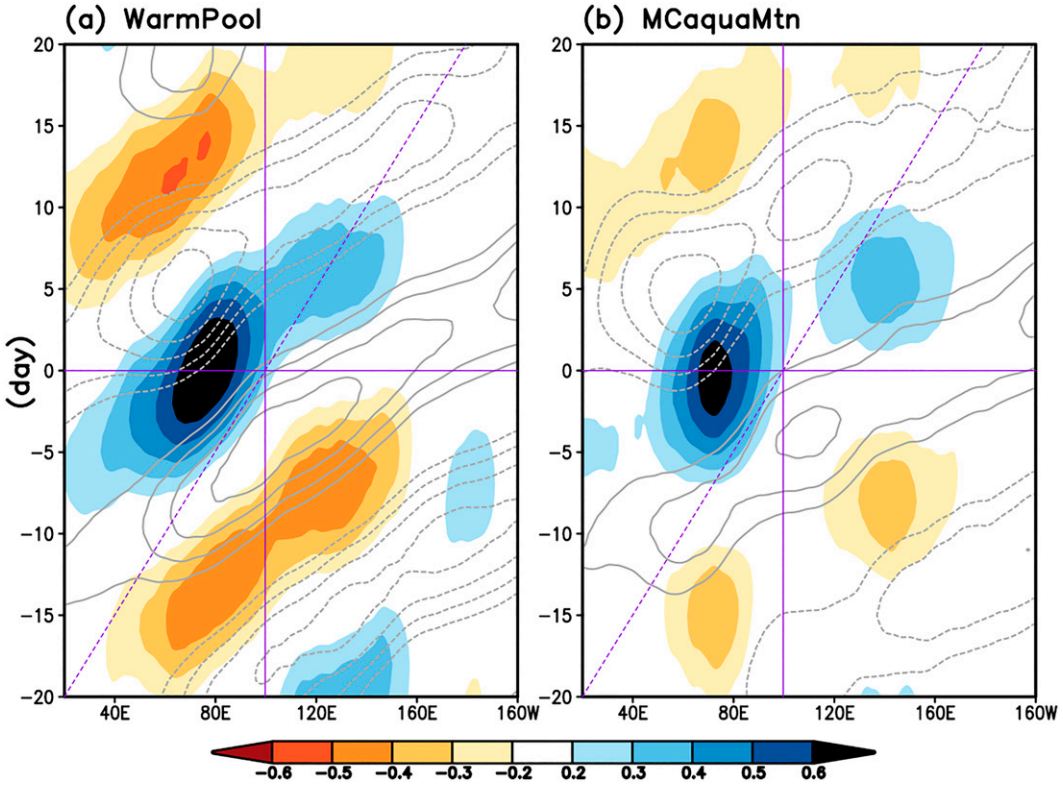

FIG. 9. Lag–longitude evolution of correlation coefficients of anomalous OLR (W m^{-2}: shading) and U850 (m s^{-1}; contour interval: 0.2, starting from 0.2) in (a) WarmPool and (b) MCaquaMtn runs. The lag correlation coefficient of 20–100-day bandpass-filtered anomalies against OLR averaged over the equatorial eastern Indian Ocean (10°S–10°N, 60°–90°E) is displayed. Coefficients are averaged over 10°S–10°N. Purple dashed lines denote the 5 m s^{-1} phase speed, which is close to the observed MJO phase speed. Purple solid lines indicate 0 lag and 100°E, respectively.

MCaquaMtn (box-and-whisker plots in Fig. 11). Note that the BCOR skill difference between WarmPool and MCaquaMtn is larger when MJO is initially located in the west of the MC (phases 2 and 3) than the western Pacific (phases 5 and 6) (not shown). This is mainly due to the higher skill of the MCaquaMtn run as they do not encounter the MC when initialized over the western Pacific. However, due to the limited sample size, we show the results of all phases rather than dividing them into eight phases.

The BMSE grows rapidly and reaches the 2.0 line (arbitrarily chosen threshold) at day 18 in the MCaquaMtn simulation, about 10 days earlier than for WarmPool (Fig. 11b). In WarmPool run, MJO forecast signal (variability of ensemble-mean) gradually decreases and reaches the 2.0 line (arbitrarily chosen threshold) at day 38. The signal decreases faster in the MCaquaMtn and reaches the threshold at day 32 (Fig. 11b). The forecast noise (ensemble spread) is rather comparable until four weeks, when it becomes slightly smaller in the MCaquaMtn. Theoretically, small ensemble spread indicates high forecast confidence and large spread indicates low confidence. The ensemble spread (i.e., noise) and ensemble-mean error (i.e., BMSE) diagnostics together provides a reliability measure, that is at what forecast lead time the ensemble forecasts are over- or underdispersive, hence unreliable. If an ensemble system is perfect with a large sample of forecasts, the error and spread is considered to be equal (Weisheimer et al. 2011). In both WarmPool and MCaquaMtn, the BMSE consistently exceeds the noise, indicating that both ensemble forecast systems are underdispersive (Fig. 11b). The gap between the BMSE and noise becomes larger in the MCaquaMtn than WarmPool, meaning that the ensemble forecast system becomes less reliable by adding the MC barrier. Given that the MJO forecasts in current S2S models are mostly underdispersive (Kim et al. 2018), improving the exaggerated MC barrier effect could reduce the gap between ensemble spread and error, thus enhancing the reliability of the ensemble systems.

Another question we want to address is whether the MC is an intrinsic MJO predictability barrier or not. Studies have shown prediction skill decrease by the exaggerated MC barrier effect, but MJO predictability is not influenced by the MC barrier (Neena et al. 2014; Kim et al. 2014). These studies were based on initialized dynamical forecasting systems, thus forecasts are contaminated by both model and initial condition error. To examine whether the MC acts as a barrier for intrinsic predictability of MJO, we perform the same perpetual and perfect-model ensemble forecast experiment as shown in Fig. 10, but with MCaquaMtn SST prescribed to both runs. In step 1, the truth is the perpetual run with the MCaquaMtn

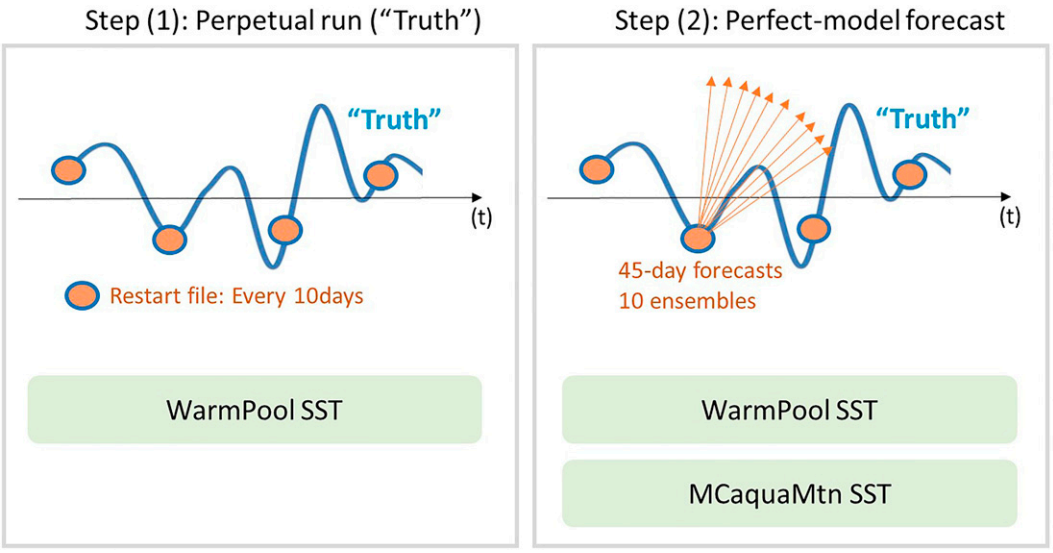

FIG. 10. Schematic of experiments: (left) step 1 is the perpetual runs and (right) step 2 is the perfect-model ensemble forecast experiment. The blue line represents the 10-yr perpetual simulation, which is regarded as "truth." Orange dots are the restart files output every 10 days, which are used for initial conditions in step 2. Orange arrows are the 10 ensembles of 45-day forecasts. Green shading represents the prescribed SST.

SST, and in step 2 the perfect-model ensemble forecast is performed with MCaquaMtn SST as well. All other processes are the same as shown in Fig. 10. By comparing the ensemble forecasts with the truth (both with MCaquaMtn SST prescribed), we can examine the MJO predictability, i.e., the model's capability to predict itself when the MC barrier exists. The forecast skill (BCOR) is shown in Fig. 11a as gray line. The predictability is close to the predictability with WarmPool SST (blue line), indicating the model is able to predict itself whether MJO is propagating or disrupted by the MC barrier. This confirms the conclusions from previous studies that the MC is not acting as an intrinsic predictability barrier of MJO, but as a prediction barrier due to the model inability in capturing the MJO propagation. The results from this study, altogether, indicate that the existence of the MC itself does not reduce the MJO predictability. However, the exaggerated MC barrier in numerical models, i.e., the inability of models in forecasting the MJO propagation, reduces the MJO prediction skill for about 1.5 weeks.

5. Summary

This study revisits the MJO predictability with perfect-model assumption, which has not been investigated for almost two decades. We provide an update of the MJO predictability using a state-of-the-art GCM that simulates a reasonable MJO and mean state. We conducted experiments with the Community Earth System Model (CESM) version 2—the latest version of the model—in its aquaplanet configuration. To examine the impact of the Maritime Continent barrier on MJO predictability and prediction skill, we have performed perfect-model forecast experiments with several different patterns of prescribed SSTs. When a tropical SST distribution approximating the observed Indo-Pacific warm pool is prescribed, both basic state and tropical modes of variability become closer to the observed than simulations with zonally symmetric SST. When the MC aqua-mountain is added, the eastward propagation of the MJO is disrupted. The predictability estimates show that the intrinsic MJO predictability is approximately 6 weeks regardless of the existence of MC but reduces to 4 weeks when the forecasted MJO is blocked by the MC barrier while it propagates in reality (truth). Also, with the exaggerated MC barrier effect, the forecast error increases faster, and signal reduces faster than the WarmPool run, indicating that the forecast is less reliable.

Previous studies have argued that the current dynamical forecasting systems possess an exaggerated MC barrier effect which prevents the MJO prediction skill from reaching its potential predictability. However, the amount of skill lost due to the MC barrier—or, alternatively, the amount of MJO skill improvement we could expect from alleviating the MC barrier effect—has not been clearly addressed. This study provides a quantitative measure of predictability loss by the exaggerated MC barrier. Note that this is an idealized model study, so the experiments which are treated as truth do not represent the true nature. One implication of this study relevant to the MJO forecast community is that, if MJO propagation is better forecasted, the skill can improve by about 2.0 weeks solely by making the MJO cross over the MC. Given that the recent operational forecasts show an average of 3–4 weeks of MJO prediction skill, we can conclude that improving the propagation of the MJO across the MC could improve the MJO skill to 5–6 weeks, close to the potential predictability found in this study. Therefore, more effort on understanding and improving the MJO propagation is needed to enhance the MJO and

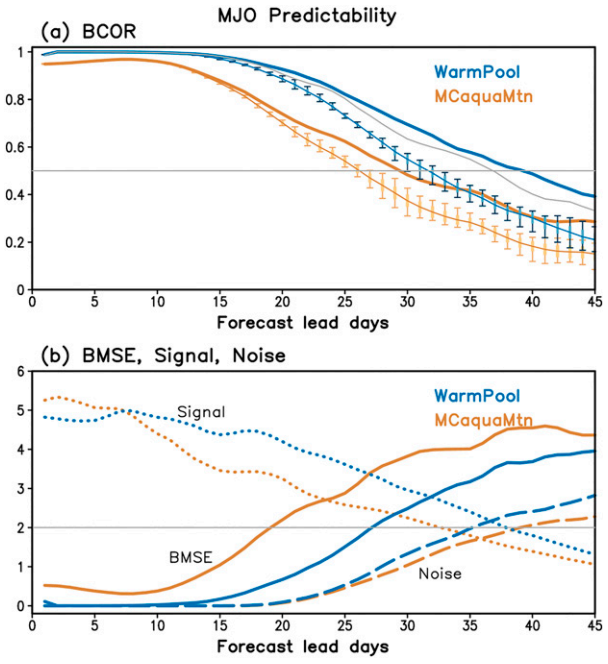

FIG. 11. MJO predictability assessed by (a) BCOR for WarmPool (blue) and MCaquaMtn (brown). The thick lines represent the skill in the ensemble mean, and the thin lines are the average of skill from individual ensembles. The box-and-whisker plots represent the spread of skill. The box outlines the ±1.0 standard deviation of skill and whiskers indicate the minimum and maximum values. The predictability measured by truth and forecasts from the MCaquaMtn SST is denoted as a gray line (discussion in section 4). (b) BMSE (solid), signal (dotted lines) and noise (dashed lines). Gray horizontal lines in (a) and (b) are arbitrarily chosen values for 0.5 and 2.0, respectively.

MJO-related forecasts to improve the overall S2S prediction. A recent field campaign and model experiments could help to address these issues (Yoneyama and Zhang 2020).

Acknowledgments. Constructive and valuable comments from three anonymous reviewers are greatly appreciated. We also thank Drs. Brian Medeiros, Daehyun Kim, and Jiyoung Han for useful discussions. H. Kim was supported by U.S. NSF Grant AGS-1652289, NOAA Grant NA22OAR4590168, NOAA Grant NA22OAR4590216, and Korean Meteorological Administration Research and Development Program under Grant KMI2021-01210. J. Benedict was supported by NSF Grant AGS-1650209. This material is based upon work supported by the National Center for Atmospheric Research (NCAR), a major facility sponsored by the NSF under Cooperative Agreement 1852977. The CESM project is supported primarily by the NSF. We would like to acknowledge high-performance computing and data storage support from Cheyenne (doi:10.5065/D6RX99HX) provided by NCAR's Computational and Information Systems Laboratory, sponsored by the NSF.

Data availability statement. ERA-Interim daily data were obtained from ECMWF: http://apps.ecmwf.int/datasets/data/interim_full_daily. Daily OLR data were downloaded from NOAA/ESRL PSD: https://www.esrl.noaa.gov/psd/data/gridded/data.interp_OLR.html. Output from CESM2 simulations are available from the corresponding author upon reasonable request.

REFERENCES

Adames, A. F., and D. Kim, 2016: The MJO as a dispersive, convectively coupled moisture wave: Theory and observations. *J. Atmos. Sci.*, **73**, 913–941, https://doi.org/10.1175/JAS-D-15-0170.1.

Ahn, M.-S., D. Kim, K. R. Sperber, I.-S. Kang, E. Maloney, D. Waliser, and H. Hendon, 2017: MJO simulation in CMIP5 climate models: MJO skill metrics and process-oriented diagnosis. *Climate Dyn.*, **49**, 4023–4045, https://doi.org/10.1007/s00382-017-3558-4.

——, and Coauthors, 2020: MJO propagation across the Maritime Continent: Are CMIP6 models better than CMIP5 models? *Geophys. Res. Lett.*, **47**, e2020GL087250, https://doi.org/10.1029/2020GL087250.

Andersen, J. A., and Z. Kuang, 2012: Moist static energy budget of MJO-like disturbances in the atmosphere of a zonally symmetric aquaplanet. *J. Climate*, **25**, 2782–2804, https://doi.org/10.1175/JCLI-D-11-00168.1.

Arnold, N. P., M. Branson, Z. Kuang, D. A. Randall, and E. Tziperman, 2015: MJO intensification with warming in the superparameterized CESM. *J. Climate*, **28**, 2706–2724, https://doi.org/10.1175/JCLI-D-14-00494.1.

Bechtold, P., M. Köhler, T. Jung, F. Doblas-Reyes, M. Leutbecher, M. J. Rodwell, F. Vitart, and G. Balsamo, 2008: Advances in simulating atmospheric variability with the ECMWF model: From synoptic to decadal time-scales. *Quart. J. Roy. Meteor. Soc.*, **134**, 1337–1351, https://doi.org/10.1002/qj.289.

Benedict, J. J., B. Medeiros, A. C. Clement, and A. G. Pendergrass, 2017: Sensitivities of the hydrologic cycle to model physics, grid resolution, and ocean type in the aquaplanet Community Atmosphere Model. *J. Adv. Model. Earth Syst.*, **9**, 1307–1324, https://doi.org/10.1002/2016MS000891.

Bretherton, C. S., M. E. Peters, and L. E. Back, 2004: Relationships between water vapor path and precipitation over the tropical oceans. *J. Climate*, **17**, 1517–1528, https://doi.org/10.1175/1520-0442(2004)017<1517:RBWVPA>2.0.CO;2.

Bui, H. X., and E. D. Maloney, 2019: Mechanisms for global warming impacts on Madden–Julian Oscillation precipitation amplitude. *J. Climate*, **32**, 6961–6975, https://doi.org/10.1175/JCLI-D-19-0051.1.

Capotondi, A., C. Deser, A. S. Phillips, Y. Okumura, and S. M. Larson, 2020: ENSO and Pacific decadal variability in the Community Earth System Model version 2. *J. Adv. Model. Earth Syst.*, **12**, e2019MS002022, https://doi.org/10.1029/2019MS002022.

Chen, G., J. Ling, C. Li, Y. Zhang, and C. Zhang, 2020: Barrier effect of the Indo-Pacific Maritime Continent on MJO propagation in observations and CMIP5 models. *J. Climate*, **33**, 5173–5193, https://doi.org/10.1175/JCLI-D-19-0771.1.

——, ——, R. Zhang, Z. Xiao, and C. Li, 2022: The MJO from CMIP5 to CMIP6: Perspectives from tracking MJO precipitation. *Geophys. Res. Lett.*, **49**, e2021GL095241, https://doi.org/10.1029/2021GL095241.

Danabasoglu, G., and Coauthors, 2020: The Community Earth System Model version 2 (CESM2). *J. Adv. Model. Earth Syst.*, **12**, e2019MS001916, https://doi.org/10.1029/2019MS001916.

Das, S., D. Sengupta, and A. Chakraborty, 2019: The Madden–Julian oscillation in an aquaplanet-like general circulation model with and without continents. *J. Adv. Model. Earth Syst.*, **11**, 1459–1476, https://doi.org/10.1029/2018MS001455.

Dee, D. P., and Coauthors, 2011: The ERA-Interim reanalysis: Configuration and performance of the data assimilation system. *Quart. J. Roy. Meteor. Soc.*, **137**, 553–597, https://doi.org/10.1002/qj.828.

DeMott, C. A., D. A. Randall, and M. Khairoutdinov, 2007: Convective precipitation variability as a tool for general circulation model analysis. *J. Climate*, **20**, 91–112, https://doi.org/10.1175/JCLI3991.1.

——, N. P. Klingaman, and S. J. Woolnough, 2015: Atmosphere–ocean coupled processes in the Madden–Julian oscillation. *Rev. Geophys.*, **53**, 1099–1154, https://doi.org/10.1002/2014RG000478.

Feng, J., T. Li, and W. Zhu, 2015: Propagating and nonpropagating MJO events over Maritime Continent. *J. Climate*, **28**, 8430–8449, https://doi.org/10.1175/JCLI-D-15-0085.1.

Gonzalez, A. O., and X. Jiang, 2017: Winter mean lower tropospheric moisture over the Maritime Continent as a climate model diagnostic metric for the propagation of the Madden–Julian oscillation. *Geophys. Res. Lett.*, **44**, 2588–2596, https://doi.org/10.1002/2016GL072430.

Hagos, S. M., C. Zhang, Z. Feng, C. D. Burleyson, C. De Mott, B. Kerns, J. J. Benedict, and M. N. Martini, 2016: The impact of the diurnal cycle on the propagation of Madden–Julian Oscillation convection across the Maritime Continent. *J. Adv. Model. Earth Syst.*, **8**, 1552–1564, https://doi.org/10.1002/2016MS000725.

Hannah, W. M., and E. D. Maloney, 2014: The moist static energy budget in NCAR CAM5 hindcasts during DYNAMO. *J. Adv. Model. Earth Syst.*, **6**, 420–440, https://doi.org/10.1002/2013MS000272.

Hirons, L. C., P. Inness, F. Vitart, and P. Bechtold, 2013a: Understanding advances in the simulation of intraseasonal variability in the ECMWF model. Part I: The representation of the MJO. *Quart. J. Roy. Meteor. Soc.*, **139**, 1417–1426, https://doi.org/10.1002/qj.2060.

——, ——, ——, and ——, 2013b: Understanding advances in the simulation of intraseasonal variability in the ECMWF model. Part II: The application of process-based diagnostics. *Quart. J. Roy. Meteor. Soc.*, **139**, 1427–1444, https://doi.org/10.1002/qj.2059.

Hoskins, B., R. Neale, M. Rodwell, and G.-Y. Yang, 1999: Aspects of the large-scale tropical atmospheric circulation. *Tellus*, **51A**, 33–44, https://doi.org/10.3402/tellusa.v51i1.12287.

Hsu, P.-C., T. Li, and H. Murakami, 2014: Moisture asymmetry and MJO eastward propagation in an aquaplanet general circulation model. *J. Climate*, **27**, 8747–8760, https://doi.org/10.1175/JCLI-D-14-00148.1.

Huffman, G. J., R. F. Adler, M. M. Morrissey, D. T. Bolvin, S. Curtis, R. Joyce, B. McGavock, and J. Susskind, 2001: Global precipitation at one-degree daily resolution from multisatellite observations. *J. Hydrometeor.*, **2**, 36–50, https://doi.org/10.1175/1525-7541(2001)002<0036:GPAODD>2.0.CO;2.

Inness, P. M., and J. M. Slingo, 2006: The interaction of the Madden–Julian Oscillation with the Maritime Continent in a GCM. *Quart. J. Roy. Meteor. Soc.*, **132**, 1645–1667, https://doi.org/10.1256/qj.05.102.

——, J. M. Slingo, S. J. Woolnough, R. B. Neale, and V. D. Pope, 2001: Organization of tropical convection in a GCM with varying vertical resolution; implications for the simulation of the Madden–Julian oscillation. *Climate Dyn.*, **17**, 777–793, https://doi.org/10.1007/s003820000148.

Jiang, X., 2017: Key processes for the eastward propagation of the Madden–Julian oscillation based on multimodel simulations. *J. Geophys. Res. Atmos.*, **122**, 755–770, https://doi.org/10.1002/2016JD025955.

——, and Coauthors, 2015: Vertical structure and physical processes of the Madden–Julian oscillation: Exploring key model physics in climate simulations. *J. Geophys. Res. Atmos.*, **120**, 4718–4748, https://doi.org/10.1002/2014JD022375.

——, E. Maloney, and H. Su, 2020a: Large-scale controls of propagation of the Madden–Julian oscillation. *npj Climate Atmos. Sci.*, **3**, 29, https://doi.org/10.1038/s41612-020-00134-x.

——, and Coauthors, 2020b: Fifty years of research on the Madden–Julian oscillation: Recent progress, challenges, and perspectives. *J. Geophys. Res. Atmos.*, **125**, e2019JD030911, https://doi.org/10.1029/2019JD030911.

Kang, I.-S., F. Liu, M.-S. Ahn, Y.-M. Yang, and B. Wang, 2013: The role of SST structure in convectively coupled Kelvin–Rossby waves and its implications for MJO formation. *J. Climate*, **26**, 5915–5930, https://doi.org/10.1175/JCLI-D-12-00303.1.

Kerns, B. W., and S. S. Chen, 2016: Large-scale precipitation tracking and the MJO over the Maritime Continent and Indo-Pacific warm pool. *J. Geophys. Res. Atmos.*, **121**, 8755–8776, https://doi.org/10.1002/2015JD024661.

Kim, D., A. H. Sobel, and I.-S. Kang, 2011: A mechanism denial study on the Madden–Julian oscillation. *J. Adv. Model. Earth Syst.*, **3**, M12007, https://doi.org/10.1029/2011MS000081.

——, E. D. Maloney, and C. Zhang, 2021: Review: MJO propagation over the Maritime Continent. *The Multiscale Global Monsoon System*, 4th ed., C.-P. Chang et al., Eds., World Scientific Series on Asia-Pacific Weather and Climate, Vol. 11, World Scientific, 261–272, https://doi.org/10.1142/9789811216602_0021.

Kim, H., 2017: The impact of the mean moisture bias on the key physics of MJO propagation in the ECMWF reforecast. *J. Geophys. Res. Atmos.*, **122**, 7772–7784, https://doi.org/10.1002/2017JD027005.

——, P. J. Webster, V. E. Toma, and D. Kim, 2014: Predictability and prediction skill of the MJO in two operational forecasting systems. *J. Climate*, **27**, 5364–5378, https://doi.org/10.1175/JCLI-D-13-00480.1.

——, F. Vitart, and D. E. Waliser, 2018: Prediction of the Madden–Julian oscillation: A review. *J. Climate*, **31**, 9425–9443, https://doi.org/10.1175/JCLI-D-18-0210.1.

——, M. A. Janiga, and K. Pegion, 2019: MJO propagation processes and mean biases in the SubX and S2S reforecasts. *J. Geophys. Res. Atmos.*, **124**, 9314–9331, https://doi.org/10.1029/2019JD031139.

——, Y. G. Ham, Y. S. Joo, and S. W. Son, 2021: Deep learning for bias correction of MJO prediction. *Nat. Commun.*, **12**, 3087, https://doi.org/10.1038/s41467-021-23406-3.

Leroux, S., and Coauthors, 2016: Inter-model comparison of subseasonal tropical variability in aquaplanet experiments: Effect of a warm pool. *J. Adv. Model. Earth Syst.*, **8**, 1526–1551, https://doi.org/10.1002/2016MS000683.

Liebmann, B., and C. A. Smith, 1996: Description of a complete (interpolated) outgoing longwave radiation dataset. *Bull. Amer. Meteor. Soc.*, **77**, 1275–1277, https://doi.org/10.1175/1520-0477-77.6.1274.

Liess, S., D. E. Waliser, and S. D. Schubert, 2005: Predictability studies of the intraseasonal oscillation with the ECHAM5 GCM. *J. Atmos. Sci.*, **62**, 3320–3336, https://doi.org/10.1175/JAS3542.1.

Lim, Y., S.-W. Son, and D. Kim, 2018: MJO prediction skill of the subseasonal-to-seasonal prediction models. *J. Climate*, **31**, 4075–4094, https://doi.org/10.1175/JCLI-D-17-0545.1.

Ling, J., C. Zhang, R. Joyce, P.-P. Xie, and G. Chen, 2019: Possible role of the diurnal cycle in land convection in the barrier effect on the MJO by the Maritime Continent. *Geophys. Res. Lett.*, **46**, 3001–3011, https://doi.org/10.1029/2019GL081962.

Liu, X., and Coauthors, 2017: MJO prediction using the subseasonal to seasonal forecast model of Beijing Climate Center. *Climate Dyn.*, **48**, 3283–3307, https://doi.org/10.1007/s00382-016-3264-7.

Madden, R., and P. Julian, 1972: Further evidence of global-scale, 5-day pressure waves. *J. Atmos. Sci.*, **29**, 1464–1469, https://doi.org/10.1175/1520-0469(1972)029<1464:FEOGSD>2.0.CO;2.

Maloney, E. D., and A. H. Sobel, 2004: Surface fluxes and ocean coupling in the tropical intraseasonal oscillation. *J. Climate*, **17**, 4368–4386, https://doi.org/10.1175/JCLI-3212.1.

——, and B. O. Wolding, 2015: Initiation of an intraseasonal oscillation in an aquaplanet general circulation model. *J. Adv. Model. Earth Syst.*, **7**, 1956–1976, https://doi.org/10.1002/2015MS000495.

——, A. H. Sobel, and W. M. Hannah, 2010: Intraseasonal variability in an aquaplanet general circulation model. *J. Adv. Model. Earth Syst.*, **2**, 5, https://doi.org/10.3894/JAMES.2010.2.5.

Mariotti, A., and Coauthors, 2020: Windows of opportunity for skillful forecasts subseasonal to seasonal and beyond. *Bull. Amer. Meteor. Soc.*, **101**, E608–E625, https://doi.org/10.1175/BAMS-D-18-0326.1.

Martin, Z., S.-W. Son, A. Butler, H. Hendon, H. Kim, A. Sobel, S. Yoden, and C. Zhang, 2021: The influence of the quasi-biennial oscillation on the Madden–Julian oscillation. *Nat. Rev. Earth Environ.*, **2**, 477–489, https://doi.org/10.1038/s43017-021-00173-9.

Medeiros, B., 2020: Aquaplanets as a framework for examination of aerosol effects. *J. Adv. Model. Earth Syst.*, **12**, e2019MS001874, https://doi.org/10.1029/2019MS001874.

Neale, R. B., and B. J. Hoskins, 2000: A standard test for AGCMs including their physical parametrizations: I: The proposal. *Atmos. Sci. Lett.*, **1**, 101–107, https://doi.org/10.1006/asle.2000.0022.

Neale, R., and J. Slingo, 2003: The Maritime Continent and its role in the global climate: A GCM study. *J. Climate*, **16**, 834–848, https://doi.org/10.1175/1520-0442(2003)016<0834:TMCAIR>2.0.CO;2.

Neena, J. M., J. Y. Lee, D. Waliser, B. Wang, and X. Jiang, 2014: Predictability of the Madden–Julian oscillation in the Intraseasonal Variability Hindcast Experiment (ISVHE). *J. Climate*, **27**, 4531–4543, https://doi.org/10.1175/JCLI-D-13-00624.1.

Peatman, S. C., A. J. Matthews, and D. P. Stevens, 2014: Propagation of the Madden–Julian oscillation through the Maritime Continent and scale interaction with the diurnal cycle of precipitation. *Quart. J. Roy. Meteor. Soc.*, **140**, 814–825, https://doi.org/10.1002/qj.2161.

——, J. Methven, and S. J. Woolnough, 2018: Isolating the effects of moisture entrainment on convectively coupled equatorial waves in an aquaplanet GCM. *J. Atmos. Sci.*, **75**, 3139–3157, https://doi.org/10.1175/JAS-D-18-0098.1.

Pegion, K., and Coauthors, 2019: The Subseasonal Experiment (SubX): A multimodel subseasonal prediction experiment. *Bull. Amer. Meteor. Soc.*, **100**, 2043–2060, https://doi.org/10.1175/BAMS-D-18-0270.1.

Pritchard, M. S., and D. Yang, 2016: Response of the superparameterized Madden–Julian oscillation to extreme climate and basic-state variation challenges a moisture mode view. *J. Climate*, **29**, 4995–5008, https://doi.org/10.1175/JCLI-D-15-0790.1.

Rayner, N. A., D. E. Parker, E. B. Horton, C. K. Folland, L. V. Alexander, D. P. Rowell, E. C. Kent, and A. Kaplan, 2003: Global analyses of sea surface temperature, sea ice, and night marine air temperature since the late nineteenth century. *J. Geophys. Res.*, **108**, 4407, https://doi.org/10.1029/2002JD002670.

Roundy, P. E., 2012: Observed structure of convectively coupled waves as a function of equivalent depth: Kelvin waves and the Madden–Julian oscillation. *J. Atmos. Sci.*, **69**, 2097–2106, https://doi.org/10.1175/JAS-D-12-03.1.

Rui, H., and B. Wang, 1990: Development characteristics and dynamic structure of tropical intraseasonal convection anomalies. *J. Atmos. Sci.*, **47**, 357–379, https://doi.org/10.1175/1520-0469(1990)047<0357:DCADSO>2.0.CO;2.

Rushley, S. S., D. Kim, C. S. Bretherton, and M.-S. Ahn, 2018: Reexamining the nonlinear moisture-precipitation relationship over the tropical oceans. *Geophys. Res. Lett.*, **45**, 1133–1140, https://doi.org/10.1002/2017GL076296.

Sardeshmukh, P. D., and B. J. Hoskins, 1988: The generation of global rotational flow by steady idealized tropical divergence. *J. Atmos. Sci.*, **45**, 1228–1251, https://doi.org/10.1175/1520-0469(1988)045<1228:TGOGRF>2.0.CO;2.

Shi, X., D. Kim, Á. F. Adames, and J. Sukhatme, 2018: WISHE-moisture mode in an aquaplanet simulation. *J. Adv. Model. Earth Syst.*, **10**, 2393–2407, https://doi.org/10.1029/2018MS001441.

Simpson, I. R., and Coauthors, 2020: An evaluation of the large-scale atmospheric circulation and its variability in CESM2 and other CMIP models. *J. Geophys. Res. Atmos.*, **125**, e2020JD032835, https://doi.org/10.1029/2020JD032835.

Sobel, A. H., and E. Maloney, 2012: An idealized semi-empirical framework for modeling the Madden–Julian oscillation. *J. Atmos. Sci.*, **69**, 1691–1705, https://doi.org/10.1175/JAS-D-11-0118.1.

——, and ——, 2013: Moisture modes and the eastward propagation of the MJO. *J. Atmos. Sci.*, **70**, 187–192, https://doi.org/10.1175/JAS-D-12-0189.1.

——, E. D. Maloney, G. Bellon, and D. M. Frierson, 2010: Surface fluxes and tropical intraseasonal variability: A reassessment. *J. Adv. Model. Earth Syst.*, **2**, 2, https://doi.org/10.3894/JAMES.2010.2.2.

Tan, H., P. Ray, B. Barrett, M. Tewari, and M. Moncrieff, 2020: Role of topography on the MJO in the Maritime Continent: A numerical case study. *Climate Dyn.*, **55**, 295–314, https://doi.org/10.1007/s00382-018-4275-3.

Tseng, W., H. Hsu, N. Keenlyside, C. J. Chang, B. Tsuang, C. Tu, and L. Jiang, 2017: Effects of surface orography and land–sea contrast on the Madden–Julian oscillation in the Maritime Continent: A numerical study using ECHAM5-SIT. *J. Climate*, **30**, 9725–9741, https://doi.org/10.1175/JCLI-D-17-0051.1.

Vitart, F., 2014: Evolution of ECMWF sub-seasonal forecast skill scores. *Quart. J. Roy. Meteor. Soc.*, **140**, 1889–1899, https://doi.org/10.1002/qj.2256.

——, 2017: Madden–Julian oscillation prediction and teleconnections in the S2S database. *Quart. J. Roy. Meteor. Soc.*, **143**, 2210–2220, https://doi.org/10.1002/qj.3079.

——, and Coauthors, 2017: The Subseasonal to Seasonal (S2S) Prediction project database. *Bull. Amer. Meteor. Soc.*, **98**, 163–173, https://doi.org/10.1175/BAMS-D-16-0017.1.

Waliser, D. E., K. M. Lau, W. Stern, and C. Jones, 2003: Potential predictability of the Madden–Julian oscillation. *Bull. Amer. Meteor. Soc.*, **84**, 33–50, https://doi.org/10.1175/BAMS-84-1-33.

Wang, S., and A. H. Sobel, 2022: A unified moisture mode theory for the Madden–Julian oscillation and the boreal summer intraseasonal oscillation. *J. Climate*, **35**, 1267–1291, https://doi.org/10.1175/JCLI-D-21-0361.1.

——, ——, M. K. Tippett, and F. Vitart, 2019: Prediction and predictability of tropical intraseasonal convection: Seasonal dependence and the Maritime Continent prediction barrier. *Climate Dyn.*, **52**, 6015–6031, https://doi.org/10.1007/s00382-018-4492-9.

Weisheimer, A., T. N. Palmer, and F. J. Doblas-Reyes, 2011: Assessment of representations of model uncertainty in monthly and seasonal forecast ensembles. *Geophys. Res. Lett.*, **38**, L16703, https://doi.org/10.1029/2011GL048123.

Wheeler, M., and G. N. Kiladis, 1999: Convectively coupled equatorial waves: Analysis of clouds and temperature in the wavenumber–frequency domain. *J. Atmos. Sci.*, **56**, 374–399, https://doi.org/10.1175/1520-0469(1999)056<0374:CCEWAO>2.0.CO;2.

Wheeler, M. C., and H. H. Hendon, 2004: An all-season real-time multivariate MJO index: Development of an index for monitoring and prediction. *Mon. Wea. Rev.*, **132**, 1917–1932, https://doi.org/10.1175/1520-0493(2004)132<1917:AARMMI>2.0.CO;2.

Williamson, D. L., and Coauthors, 2013: The Aqua-Planet Experiment (APE): Response to changed meridional SST profile. *J. Meteor. Soc. Japan*, **91A**, 57–89, https://doi.org/10.2151/jmsj.2013-A03.

Wu, C.-H., and H.-H. Hsu, 2009: Topographic influence on the MJO in the Maritime Continent. *J. Climate*, **22**, 5433–5448, https://doi.org/10.1175/2009JCLI2825.1.

Wu, X., K. A. Reed, C. L. P. Wolfe, G. M. Marques, S. D. Bachman, and F. O. Bryan, 2021: The dependence of tropical modes of variability on zonal asymmetry. *Geophys. Res. Lett.*, **48**, e2021GL093966, https://doi.org/10.1029/2021GL093966.

Xiang, B., and Coauthors, 2022: S2S prediction in GFDL SPEAR: MJO diversity and teleconnections. *Bull. Amer. Meteor. Soc.*, **103**, E463–E484, https://doi.org/10.1175/BAMS-D-21-0124.1.

Yoneyama, K., and C. Zhang, 2020: Years of the Maritime Continent. *Geophys. Res. Lett.*, **47**, e2020GL087182, https://doi.org/10.1029/2020GL087182.

Zhang, C., and J. Ling, 2017: Barrier effect of the Indo-Pacific Maritime Continent on the MJO: Perspectives from tracking MJO precipitation. *J. Climate*, **30**, 3439–3459, https://doi.org/10.1175/JCLI-D-16-0614.1.

——, Á. F. Adames, B. Khouider, B. Wang, and D. Yang, 2020: Four theories of the Madden–Julian oscillation. *Rev. Geophys.*, **58**, e2019RG000685, https://doi.org/10.1029/2019RG000685.

Zhang, G. J., and N. A. McFarlane, 1995: Sensitivity of climate simulations to the parameterization of cumulus convection in the Canadian Climate Centre general circulation model. *Atmos.–Ocean*, **33**, 407–446, https://doi.org/10.1080/07055900.1995.9649539.

Zhou, Y., J. Fang, and S. Wang, 2021: Impact of islands on the MJO propagation across the Maritime Continent: A numerical modeling study of an MJO event. *Climate Dyn.*, **57**, 2921–2935, https://doi.org/10.1007/s00382-021-05849-y.